Symmetry considerations on band filling and first optical transition in NiO

John E. Petersen, Luisa M. Scolfaro, Pablo D. Borges and Wilhelmus J. Geerts

Regular Article

Symmetry considerations on band filling and first optical transition in NiO

John E. Petersen[1,a], Luisa M. Scolfaro[1], Pablo D. Borges[1,2], and Wilhelmus J. Geerts[1]

[1] Department of Physics, Texas State University, 78666 San Marcos, TX, USA
[2] Instituto de Ciencias Exatas e Tecnologia, Universidade Federal de Vicosa, Campus de Rio Paranaíba, Rio Paranaíba, 38810-000 MG, Brazil

Abstract. Recent theoretical works on NiO have not agreed upon the nature of the first optical transition. By altering band filling – with highly concentrated O vacancies and Fe impurities – here, the orbital density of states is changed near the Fermi energy. The variation in optical properties, relative to the changes in orbital character, along with group theory analysis of hybridized orbitals, provides new insight when evaluating the first optical transition of NiO. Here, based on density functional theory, the first optical transition is found to have two possibilities – either superexchange site-hopping or a transition from the hybridized e_g state to the hybridized a_{1u} state, rather than the intra-atomic transitions which are causing disagreement in the recent literature.

1 Introduction

In recent years, NiO_y has been studied for numerous applications ranging from use as the pseudocapacitor electrode in electrochemical supercapacitors [1,2], the spin filter in spintronics applications [3] the electrochromic (EC) material in EC devices [4], the sensing material in gas sensor devices [5], and perhaps most noteworthy, the resistive switching material in resistive random access memory (RRAM) [6–14]. The y in NiO_y represents a non-stoichiometric concentration of O, with a value less than unity indicating O vacancies or Ni precipitates, and with a value greater than unity indicating Ni vacancies or excess O interstitials. Being the functional material in all of the mentioned applications, clearly, the physical properties of NiO_y are of great interest for the next generation of electronic devices. As scaling issues become a greater concern, alternative non-volatile memory technology is sought. RRAM, particularly NiO-based RRAM, is an attractive candidate for such an application.

To be of use, understanding the science behind the switching process in RRAM is paramount. Only recently has the scientific community agreed on the mechanism behind RRAM switching. As the metal electrode scavenges O anions upon an applied threshold voltage, creating conducting filaments (CFs), this results in a Ni-rich condition where 2^+ O vacancies become increasingly more stable at higher Fermi energies (E_F) [10,15–17]. In other words, the O vacancy behaves as a 2^+ charge center

which bonds with the Ni valence. While the most stable defect in NiO is Ni vacancies which give NiO its intrinsic p-type character, the conducting filaments (CFs) within the functional material in RRAM consist of O vacancies and/or metal precipitates. Open questions, such as the O vacancy concentration within the CFs during the switching process, are studied here. We show that up to a threshold concentration of O vacancies, the system remains insulating with a substantial optical band gap.

The experimentally observed optical band gap of approximately 4.0 eV has undergone considerable theoretical scrutiny over the years, and while originally thought to be a Mott insulator, the current consensus is that NiO is either a charge-transfer insulator or possibly having characteristics of both types [12,18–24]. The gap of a Mott insulator consists of a d-d transition, as a result of exchange and crystal field splitting, whereas the gap of a charge-transfer insulator consists of a transition typically from the anion valence band to the cation conduction band [19]. The d orbitals of Ni are split into tri-degenerate t_{2g} and bi-degenerate eg states by the crystal field induced by the octahedral (O_h) coordination of Ni-O bonds in the rocksalt structure of NiO. The e_g orbitals of Ni are only partially filled, giving rise to the antiferromagnetic (AFM) nature of the material, and the t_{2g} orbitals are completely occupied. Locally, the density of states (DOS) of each Ni lies within a strong ligand field, resulting in a large splitting between the e_g and t_{2g} states, as shown previously [25]. Most works report a valence band comprised of a mix between O p and Ni t_{2g} states and a Ni e_g conduction band [12,18–24]. However, some recent works indicate that the

[a] e-mail: jepetersen@utexas.edu

lowest energy conduction band is Ni s [26,27]. Rödl et al. suggest the dispersive CBM at the Γ point is of s character [18]. In subsequent work, Rödl and Bechstedt concluded from expensive GW calculations, in conjunction with the Bethe-Salpeter equation, that the first optical transition is intra-atomic from the t_{2g} band of one Ni site to the e_g band of the same Ni [28]. They emphasize that due to the hybridization of states comprising these bands, disentangling them into a purely atomic interpretation of the first optical transition can be particularly misleading. Also, they show that density functional theory, with a Hubbard potential U (DFT + U), is particularly accurate in qualitatively describing the orbital character of the partial density of states (PDOS). For this reason, here, the PDOS is calculated within DFT + U, and rather than attempting to disentangle atomic states, hybridization is taken into account by interpreting the first optical transition within fundamental group theory and ligand field theory.

Conventional DFT is well-known to either incorrectly predict metallic behavior or greatly underestimate the energy band gap for many materials containing ions with partially-filled d or f shells – including transition metal oxides such as NiO. In many cases, materials are not found to have conduction bands or magnetic properties described correctly. Materials with partially filled d or f orbitals are said to be highly-correlated, meaning that intra-atomic correlation is particularly strong between electrons in d or f orbitals which are partially filled. In exchange-correlation approximations based on the local spin-density approximation (LSDA), such as the generalized gradient approximation (GGA) used here, spin in the electronic density function is dependent upon Hund's-rule exchange energy (J), but in Mott-like insulators, spin is predominantly dependent upon the Hubbard potential energy (U). The problem is that the Hubbard potential energy (U) is roughly an order of magnitude greater than the exchange energy [29]. Therefore, in this work, an effective Hubbard U–J Hamiltonian, following the Dudarev approach [30], is added to the GGA Hamiltonian. This method has been shown to be particularly effective at describing experimentally observed physical properties in NiO. Recently, Shin et al. were critical of the GGA+U method – however, even they agree that electronic properties are described very well in the intrinsic case of NiO and with O vacancy [31]. In order to further corroborate our conclusions, here we also performed the calculations using the Hybrid functional (HSE06) [32] for NiO, NiO_y, as well as for NiFeO and $NiFeO_y$ ($y < 1$). Despite being computationally more demanding, hybrid functionals have proven to be reliable for these systems. The results presented in this work with GGA + U are in excellent agreement with HSE06.

The disagreement in the literature mentioned above is clarified here by calculating the effects of Fe impurities and O vacancies on band filling in NiO. While the rock-salt phase of FeO is not stable at room temperature, the phase diagram of the Ni-Fe-O system reports a stable rock-salt structure for iron concentrations up to $x = 0.4$ in a low oxygen atmosphere [33]. With the sputtering vapor deposition technique, oxygen levels can be

finely tuned to achieve near-stoichiometric or oxygen-poor AFM $Ni_{1-x}Fe_xO_y$ thin films. Reports of dual ion beam sputtered $Ni_{1-x}Fe_xO$ ($x = 0.19$) and radio frequency magnetron sputtered $Ni_{1-x}Fe_xO$ confirm the rock salt crystal structure via X-ray diffraction for films sputtered at low oxygen pressure [34–36]. At lower concentrations, Wensheng et al. have found, via X-ray diffraction, a rock-salt phase for pulsed laser deposition grown $Ni_{1-x}Fe_xO$ ($x = 0.02$), as well [37].

Since Fe has two fewer 3d electrons than Ni, the stable NiFeO alloy is particularly interesting to study band filling in NiO. Introducing O vacancies has a similar effect as Fe impurities on the band structure of NiO; however, upon taking the PDOS into account, the electronic structure is actually quite different. Furthermore, both cases differ substantially from intrinsic NiO. The comparison of the electronic structure in environments of differing band filling presented here helps to clarify the confusion in the literature of the first optical transition in NiO. The PDOS can help to characterize the first optical transition, which we calculate within the independent particle approximation [38] (IPA), but this is not enough, due to entangled bands of hybridized orbitals. This hybridization gives rise to symmetry conditions which only allow certain transitions to occur within group theory. Even though DFT + U or HSE06 cannot provide exceptionally accurate eigenvalues of conduction bands, limiting quantitative conclusions, by analyzing our IPA and PDOS calculations within group theory, we are able to make important qualitative conclusions about the underlying physical nature of NiO.

2 Theoretical methods

The projector augmented wave method, as implemented in the Vienna Ab-initio Simulation Package (VASP-PAW) was used in all calculations, performed in a spin-polarized configuration, including the GGA exchange-correlation functional of Perdew, Berke, and Ernzenhof (PBE) [39,40]. Ni $4s^23d^8$, Fe $4s^23d^6$, and O $2s^22p^4$ electrons were treated as valence in the PBE-generated PAWs, whereas inner orbitals were taken to be frozen in the core. Cutoff energy was chosen to be 520 eV, where plane waves with kinetic energy larger than the cutoff energy are excluded from the calculation. A $4 \times 4 \times 4$ gamma-centered k-point mesh was used to calculate the ground state in 32 atom $2 \times 2 \times 2$ cells, grown along the [111] cubic direction in order to simulate the AFM NiO. The 32 atom cell was used in even the intrinsic case in order to compare directly with cases with O vacancies and/or Fe dopants. An effective U–J value of 5.3 eV for both Ni and Fe was used in all calculations, because previous theoretical works have found this value to give excellent quantitative agreement with physical properties found experimentally, such as the magnetic moment of Ni, band gap, and lattice parameter [13,41]. The HSE06 approach has been adopted in the hybrid functional calculations which were performed using only the Γ-point [32].

Due to Fe having greater magnetic susceptibility than Ni, an even number of Fe must be present in the unit cell to

ensure a net magnetic moment of zero in the AFM system. Therefore, the Fe concentration of $x = 0.125$ corresponds to two Fe atoms in the unit cell. Ground state energy was calculated within the collinear spin approach, adding one Fe at a time to all possible lattice sites, in order to obtain the atomic positions of the most thermodynamically stable configuration, where Fe replaced Ni directly. The supercell underwent ionic relaxation to reduce forces on each ion to $<20\,\mathrm{meV/\AA}$. After full ionic and electronic relaxations, the energy-dependent real and imaginary parts of the complex dielectric function, for each case, were calculated within the independent-particle approximation (IPA) [38]. Further, static dielectric constants were calculated within Density Functional Perturbation Theory (DFPT) [42].

3 Results

3.1 Electronic structure

The lattice parameter, a_0, was optimized by varying the value sufficiently, fitting to the Birch-Murnaghan equation of State [43], where $a_0 = \frac{1}{2}(16V_0)^{1/3}$ or 4.189 Å, comparing favorably with the experimental value of 4.17 Å [44]. As shown previously, the calculated band structure indicates an indirect band gap for NiO, from the valence band maximum (VBM) at the T-symmetry point to the Γ-point of 3.26 eV and 4.65 eV obtained using GGA+U and HSE06 functionals, respectively, in good agreement with experiment ($\sim$3.4–4.3 eV) [25]. The PDOS calculated for pristine NiO is depicted in Figure 1. From a pure crystal-field theory interpretation, Figure 1 (top) indicates that the VBM is predominantly of O p character, and the conduction band minimum (CBM) is predominantly Ni e_g, aligning with the charge-transfer insulator point-of-view. However, taking the more rigorous interpretation of ligand field theory, where overlap of transition metal d orbitals with ligand orbitals is taken into account, in O_h symmetry, it is clear that the t_{2g} orbitals conform to a π bonding set which neither interacts with the oxygen nor can be excited to anything but an antibonding π^* orbital. By decomposing the reducible representation of all possible π orbitals, as shown by Cotton [45], we get

$$\Gamma_\pi = 3t_{1g} + 3t_{2g} + 3t_{1u} + 3t_{2u}. \tag{1}$$

Of these representations, t_{2g} matches the triplet 3d orbitals of Ni with basis functions xy, xz, and yz, while t_{1u} matches the symmetry of the p orbitals of Ni. The other two representations, while possible mathematically, have no relevant physical meaning. The t_{1u} p orbitals of Ni can be excluded from π bonding, as will be made clear below, so the result is a d^3 Ni π bond of t_{2g} symmetry. As can be seen from Figure 1 (lower), a corresponding π^* orbital is not present in the PDOS above the Fermi energy. Therefore, the Ni t_{2g} π orbital cannot be the initial state of the first optical transition. It is the s, p, and d-e_g orbitals of Ni, which overlap with O p (Fig. 1 (upper)) in octahedrally-coordinated NiO, creating σ and σ^* bonds. The σ bonds take precedence over π bonding, so the Ni p orbitals are
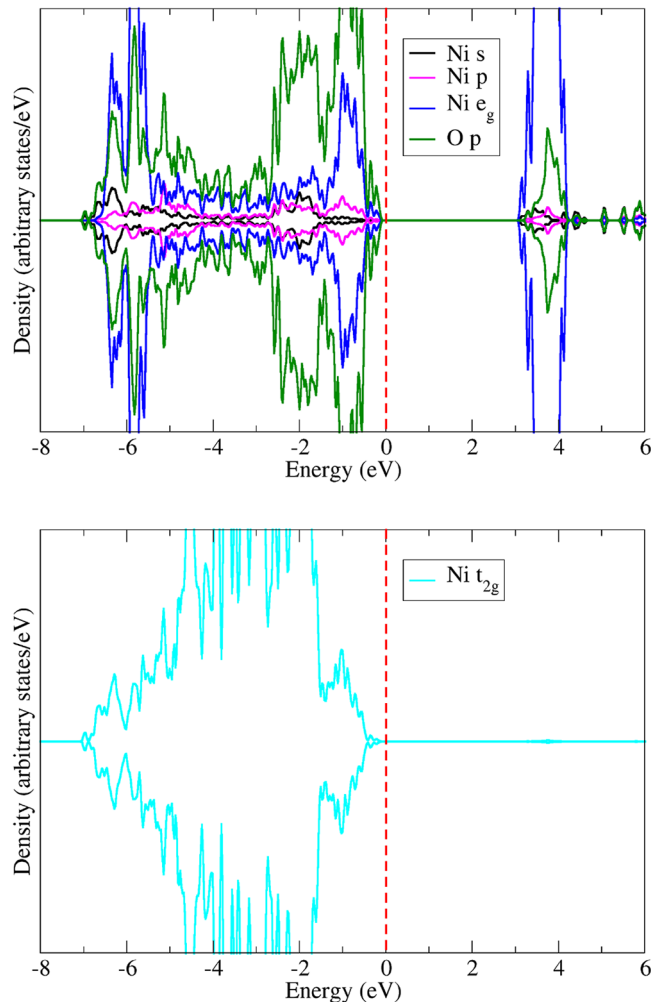

Fig. 1. Partial density of states (PDOS), per unit cell, in intrinsic NiO. The orbitals contributing to σ and σ^* bonds are shown in the upper part, and the t_{2g} orbital of Ni (lower part) is the only π bond. The Fermi energy is taken to be zero and indicated by the red dashed line.

reserved for this configuration. A similar decomposition as before, for all possible σ orbitals yields [47]

$$\Gamma_\sigma = a_{1g} + 2e_g + 3t_{1u}, \tag{2}$$

where each representation corresponds to a σ bond between O p and Ni s (a_{1g}), Ni d (e_g), and Ni p (t_{1u}). With this interpretation, the VBM at the T point is a σ orbital of e_g symmetry. Incidentally, the CBM at Γ is missing significant contribution from O p, being predominantly comprised of Ni s and Ni e_g. However, as shown previously [25], the lowest energy direct band gap is not at Γ but at T, in the Brillouin zone. For T and the other high-symmetry points, the CBM is clearly composed of a σ^* anti-bonding orbital of symmetry e_g.

Before analyzing the optical properties, it is interesting to note what happens to the t_{2g} orbital when the number of valence electrons is reduced. The $3d^6$ electrons in Fe take on a vastly different role than the $3d^8$ electrons
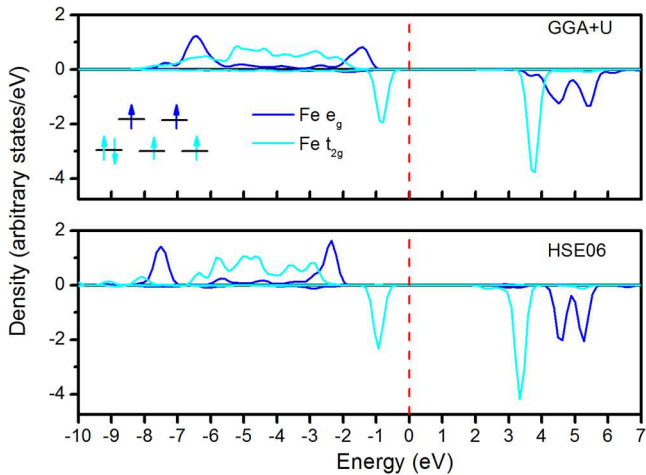
Fig. 2. Local site-projected density of states (LDOS) of the Fe impurity in an octahedral NiO crystal field, as obtained with GGA+U (top) and HSE06 (down). The d electrons of Fe are seen to split into bi-degenerate e_g and tri-degenerate t_{2g} states. The Fermi energy is taken to be zero and indicated by the red dashed line.
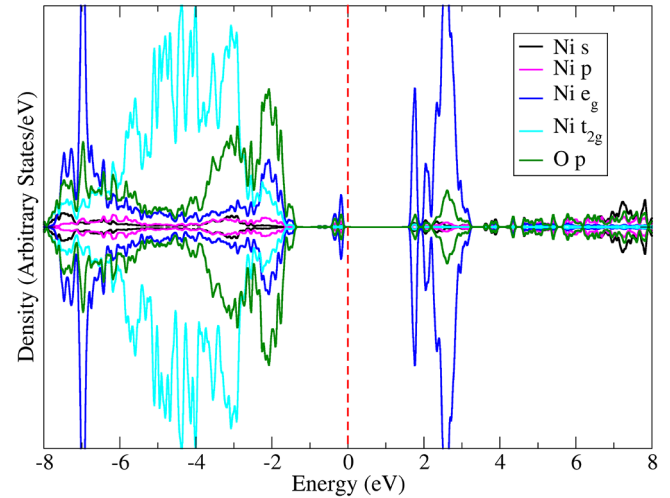

Fig. 3. Partial density of states (PDOS) of NiO with 12.5% of O vacancies. The Fermi energy is indicated by the horizontal red dashed line, taken to be zero.
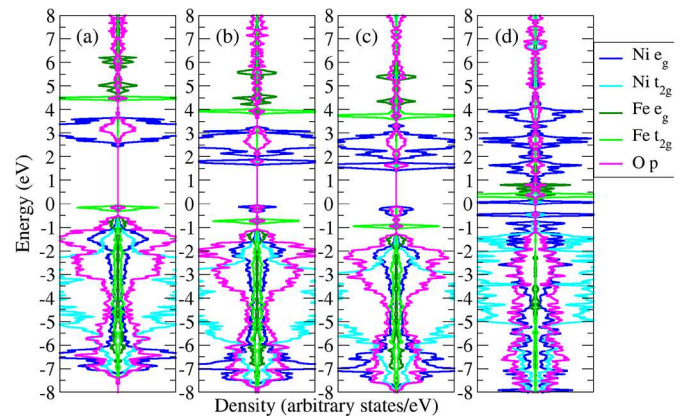

Fig. 4. Partial density of states (PDOS) of $Ni_{0.875}Fe_{0.125}O_y$ with (a) $y = 1$, (b) $y = 0.0625$, (c) $y = 0.125$, and (d) $y = 0.25$.

in Ni upon substitution in the lattice. The much larger magnetic dipole moment of Fe, 3.75 μ_B, as opposed to 1.70 μ_B of Ni, results from the high spin configuration. Figure 2 shows the PDOS of the t_{2g} and e_g orbitals of Fe. The arrows in this figure indicate the electron filling, where the three spin-up electrons in the t_{2g} symmetry form a d^3 π bond, similar to what is seen in intrinsic NiO. However, there is only one spin-down electron of t_{2g} symmetry. A highly-localized t_{2g} state is introduced with the addition of Fe at the new VBM, as we have shown previously [46]. Two spin-up e_g electrons can be seen in the LDOS, as well. Due to the increased magnetic susceptibility, without an even number of Fe impurities in the cell which are antiferromagnetically aligned, the experimentally observed net magnetization of zero would not be present.

When introducing O vacancies to NiO and NiFeO, our calculations indicate that the system remains insulating, up to a threshold concentration, somewhere between 12.5% and 25% of O sites being vacant. Figure 3 displays the PDOS of NiO with 12.5% of O vacancies, $NiO_{0.875}$, and in Figures 4a–4d we compare the PDOS of NiFeO, with 12.5% of Fe, and varying the O concentration, $Ni_{0.875}Fe_{0.125}O_y$ for $y = 1$, 0.0625, 0.125, and 0.25. The importance of these comparisons will be evident below. The key observations to note are that in both intrinsic NiO and NiFeO, when O vacancies are introduced, the vacancy-induced states of Ni e_g and O p character are fully occupied below the Fermi energy and become the VBM. Due to the higher oxidation number of Fe, O vacancies in NiFeO are more stable adjacent to Ni sites than to Fe sites, as is confirmed by our calculations where each site is tested. Thus, as with intrinsic NiO, the new VBM can be interpreted as describing the dangling e_g bonds of Ni bonding with the effectively 2+ charge-centered O vacancy.

3.2 Optical properties

The reduced band gaps in the systems considered in Figures 4a–4d do not necessarily contribute to the first optical transition, as can be seen in Figure 5. However, the lowest energy band gap of intrinsic NiO, indicated by the horizontal red dashed line in Figure 5a, does appear to coincide with the onset of the increase in the imaginary component of the dielectric function ε_2. This is also the case in Figure 5b for $NiO_{0.9375}$. Thus, the O vacancy-induced level in the valence band is responsible for the first optical transition. The characteristic optical transition at higher energy is present, as well. This characteristic transition is much broader in energy, owing to the fact that the variation in direct gaps at high symmetry points which allow a transition is larger.

Contrary to the case of the O vacancy in intrinsic NiO, when Fe is introduced to NiO as an impurity, little change in the first optical transition can be observed in Figure 5c. We reported this previously [46]; however, when O vacancies are introduced to the NiFeO system in Figure 5d, the
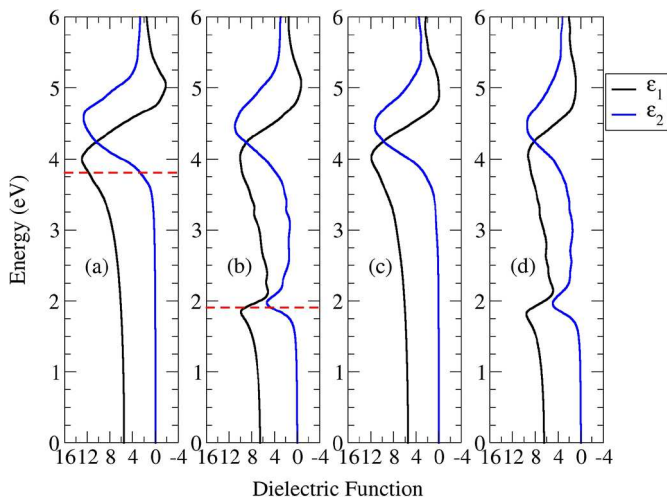
Fig. 5. Real and imaginary parts of the complex dielectric function (ε) of NiO with Fe impurities and O vacancies. From left to right, (a) displays ε of intrinsic NiO for comparison, (b) displays ε of $NiO_{0.9375}$, (c) displays ε of $Ni_{0.875}Fe_{0.125}O$, and (d) displays ε of $Ni_{0.875}Fe_{0.125}O_{0.9375}$. Horizontal red dashed lines indicate the minimum direct energy band gap in the respective material. The real portion of the dielectric function is indicated by ε_1, and the imaginary component is indicated by ε_2.
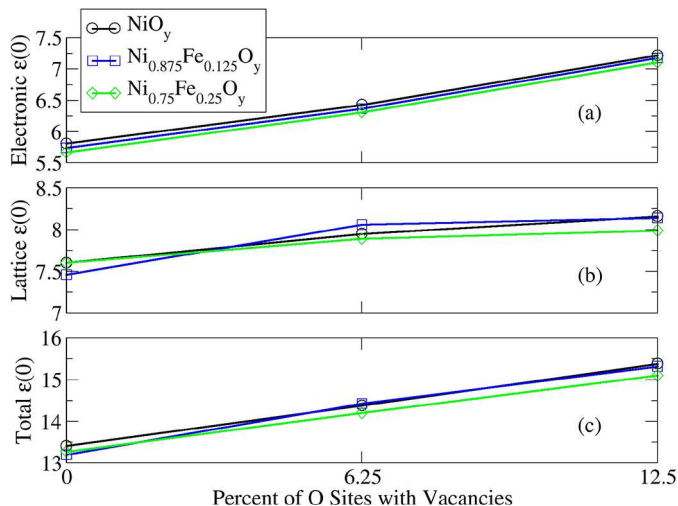
Fig. 6. Static dielectric constant of NiO with Fe impurities and O vacancies. From above to below, (a) displays the electronic contribution to the dielectric constant, calculated within the IPA, including local-field effects, (b) displays the lattice vibronic contribution to the dielectric constant, calculated within DFPT, and (c) displays the total dielectric constant, which is merely a sum of (a) and (b). Calculations were made for 0%, 6.25%, and 12.5% O vacancies for the two Fe compositions indicated in the legend.

resulting first two optical transitions are nearly identical to the case of $NiO_{0.9375}$ in Figure 5b. Note that in Figure 3 the overall electronic structure remains unaltered, yet the states are shifted lower in energy (with respect to the Fermi energy), with the fully-occupied t_{2g} state of Fe in the middle-lower of the optical gap. This confirms that the t_{2g} orbital does not contribute to the first optical transition in NiO, in agreement with the aforementioned ligand field theory prediction.

For completeness, the full static real component of the dielectric constant, $\varepsilon_{tot}(0) = \varepsilon_{latt}(0) + \varepsilon_{ele}(0)$, with the former being the lattice contribution and the latter the electronic contribution, has been calculated over a range of concentrations of O vacancies and Fe impurities and is shown in Figure 6. It is clear that both the electronic (Fig. 6a) and lattice (Fig. 6b) contributions to the dielectric constant increase with O vacancy concentration, yet the addition of Fe has little effect on this property.

4 Discussion

According to the results above, it has been clearly shown that the t_{2g} orbital of Ni does not participate in the first optical transition of NiO, so it will not be discussed further. However, from the PDOS in Figures 1 and 3, it can be seen that several states should be analyzed to determine which are allowed by selection rules. First, realizing that the perturbing Hamiltonian of the electric-dipole field of an incident electromagnetic wave is of symmetry t_{1u} in an O_h crystal-field, a direct matrix product of valence states with t_{1u} yields possible final states of allowed transitions. Rather than treat the orbitals as atomic, due to

the evident mixing of states in the valence in particular, here, they are treated as hybrid orbitals. Reducible representations were generated from the direct matrix product. Precisely to which symmetries a given symmetry is allowed to transition can be determined by the decomposition formula of group theory [45]. The following two electric-dipole transitions are possible, $t_{1u}(\sigma) \rightleftarrows t_{2g}(\pi)$ or $e_g(\sigma) \rightleftarrows t_{1u}(\sigma)$. The first possibility has been ruled out in the previous section; however, it should be mentioned that both of these possibilities are available in the PDOS. Also, the same analysis determines that the transitions between even parity states in an electric-dipole perturbative field are not possible, at least at the Γ point.

These results can be compared directly with the cases with O vacancies. In Figure 5, the first optical transition is at lower energy, due to the O vacancy-induced reduced direct band gap. The peak in ε_2 shows that this transition is narrower in energy, resulting from the localization of the CBM and narrow range of energy in the dispersion of the VBM. The dotted line indicates the narrowest direct band gap. The VBM is clearly of e_g symmetry now; so, with this interpretation, there is only one possible transition – e_g to t_{1u}.

However, another interpretation of this transition is that of site-hopping or superexchange. This is the typical description of excitation in a transition-metal oxide, where, in this case, an e_g carrier hops from one Ni site to the nearest Ni of opposite spin alignment. The transfer integral can be evaluated as being proportional to $\cos(\theta/2)$ [48], where θ is the angle between the two spins. In the simple collinear approach in this work, clearly the angle can take only one of two values – 0 or π – thus, the transition is possible only for aligned spins where kinetic

energy gain is maximized. The spin-up channel of e_g of Ni is occupied, while the spin-down channel of e_g is not. Since the nearest Ni will have opposite spin configuration, due to the magnetic ordering, this nearest Ni will have an empty e_g state of aligned spin with the occupied initial Ni e_g state. Similarly, the same argument holds for the case of an O vacancy, although the hopping distance is only from O vacancy site to nearest-neighbor Ni. The hopping mechanism between e_g states should be confirmed with calculations of exciton radius and oscillator strength of the optical transition, in terms of a Wannier-Mott exciton, where the radius of the photon-generated electron-hole pair is larger in size than the lattice spacing.

5 Conclusions

In NiFeO$_y$, the first optical transition was found by group theory analysis to involve the p orbitals of Ni, where they hybridize with p orbitals of O in an anti-bonding σ^* orbital. Within this interpretation, the first optical transition to this orbital in NiO should originate from Ni e_g hybridized with O p, which is a bonding σ orbital at the VBM. The alternative explanation is site hopping from the e_g orbital of one Ni to the e_g orbital of the next nearest Ni. This explanation is likely, due to excitons in transition metal oxides being Wannier-Mott-like with a large radius. Furthermore, it is in agreement with the observed electronic structure when including oxygen vacancies. Future excitonic calculations can confirm. It should be emphasized that group theory rules out any other optical transition when considering hybridization of orbitals.

In electronic devices, it is often the static dielectric constant which is of interest, and since iron dopants and oxygen vacancies in NiO were a large focus of this work, comparisons were made for various concentrations of both. While clearly oxygen vacancies increase the dielectric constant, addition of iron surprisingly decreases it. The effect is not large but significant; even though the static value for FeO is about twice that of NiO. The screening arising from addition of iron certainly affects the diffusion of oxygen, as well, which is critical in RRAM. Further experimental studies are encouraged to corroborate the findings predicted here.

Author contribution statement

JEP wrote the bulk of the paper, performed the bulk of the calculations, and made most of the figures. PDB performed the HSE06 calculations at a later date and added the associated text and graph. LMS and WJG were co-PIs of this work. They have helped greatly along the way in terms of scientific advice and direction.

References

1. K.-W. Nam, K.-B. Kim, J. Electrochem. Soc. **149**, A346 (2002)

2. X. Xia, J. Tu, Y. Mai, R. Chen, X. Wang, C. Gu, X. Zhao, Chem. Eur. J. **17**, 10898 (2011)

3. R. Vardimon, M. Klionsky, O. Tal, Nano Lett. **15**, 3894 (2015)

4. R.C. Korošec, P. Bukovec, Acta Chim. Slov. **53**, 136 (2006)

5. I. Hotovy, J. Huran, P. Siciliano, S. Capone, L. Spiess, V. Rehacek, Sens. Actuators B **78**, 126 (2001)

6. J.Y. Son, Y.H. Shin, Appl. Phys. Lett. **92**, 1 (2008)

7. T.G. Seong, M.R. Joung, J.W. Sun, M.K. Yang, J.K. Lee, J.W. Moon, J. Roh, S. Nahm, Jpn. J. Appl. Phys. **51**, 041102 (2012)

8. G. Ma, X. Tang, H. Zhang, Z. Zhong, J. Li, H. Su, Microelectr. Eng. **139**, 43 (2015)

9. C. Cagli, F. Nardi, D. Ielmini, IEEE Trans. Electron Devices **56**, 1712 (2009)

10. J.A. Dawson, Y. Guo, J. Robertson, Appl. Phys. Lett. **107**, 2 (2015)

11. G.S. Park, X.S. Li, D.C. Kim, R.J. Jung, M.J. Lee, S. Seo, Appl. Phys. Lett. **91**, 9 (2007)

12. H.Y. Peng, Y.F. Li, W.N. Lin, Y.Z. Wang, X.Y. Gao, T. Wu, Sci. Rep. **2**, 442 (2012)

13. S. Park, H.S. Ahn, C.K. Lee, H. Kim, H. Jin, H.S. Lee, S. Seo, J. Yu, S. Han, Phys. Rev. B **77**, 1 (2008)

14. B. Magyari-Köpe, S.G. Park, H.D. Lee, Y. Nishi, J. Mater. Sci. **47**, 7498 (2012)

15. S. Lany, J. Osorio-Guillén, A. Zunger, Phys. Rev. B **75**, 1 (2007)

16. J. Yu, K.M. Rosso, S.M. Bruemmer, J. Phys. Chem. C **116**, 1948 (2012)

17. H.D. Lee, B. Magyari-Köpe, Y. Nishi, Phys. Rev. B **81**, 1 (2010)

18. C. Rödl, F. Fuchs, J. Furthmüller, F. Bechstedt, Phys. Rev. B **79**, 1 (2009)

19. J. Zaanen, G.A. Sawatzky, J.W. Allen, Phys. Rev. Lett. **55**, 418 (1985)

20. D. Adler, J. Feinleib, Phys. Rev. B **2**, 3112 (1970)

21. A. Fujimori, F. Minami, S. Sugano, Phys. Rev. B **29**, 5225 (1984)

22. A. Fujimori, F. Minami, Phys. Rev. B **30**, 957 (1984)

23. G.A. Sawatzky, J.W. Allen, Phys. Rev. Lett. **53**, 2339 (1984)

24. J. Zaanen, G.A. Sawatzky, J. Solid State Chem. **88**, 8 (1990)

25. J. Petersen, F. Twagirayezu, P.D. Borges, L. Scolfaro, W. Geerts, MRS Adv. **1**, 2617 (2016)

26. A. Ghosh, C.M. Nelson, L.S. Abdallah, S. Zollner, J. Vac. Sci. Technol. A **33**, 061203 (2015)

27. R. Gillen, J. Robertson, J. Phys.: Condens. Matter **25**, 165502 (2013)

28. C. Rödl, F. Bechstedt, Phys. Rev. B **86**, 1 (2012)

29. V.I. Anisimov, J. Zaanen, O.K. Andersen, Phys. Rev. B **44**, 943 (1991)

30. S.L. Dudarev, S.Y. Savrasov, C.J. Humphreys, A.P. Sutton, Phys. Rev. B **57**, 1505 (1998)

31. H. Shin, Y. Luo, P. Ganesh, J. Balachandran, J.T. Krogel, P.R.C. Kent, A. Benali, O. Heinonen, Phys. Rev. Mater. **1**, 73603 (2017)

32. A.V. Krukau, O.A. Vydrov, A.F. Izmaylov, G.E. Scuseria, J. Chem. Phys. **125**, 224106 (2006)

33. V. Raghavan, J. Phase Equilib. Diffus. **31**, 369 (2010)

34. M.S. Compton, N.A. Simpson, E.G. LeBlanc, M.A. Robinson, W.J. Geerts, MRS Proc. **1708**, mrss14 (2014)

35. M.A.A. Talukder, Y. Cui, M. Compton, W. Geerts, L. Scolfaro, S. Zollner, MRS Adv. **1**, 3361 (2016)

36. A.K. Bandyopadhyay, S.E. Rios, A. Tijerina, C.J. Gutierrez, J. Alloys Compd. **369**, 217 (2004)

37. Y. Wensheng, W. Weng, G. Zhang, Z. Sun, Q. Liu, Z. Pan, Y. Guo, P. Xu, S. Wei, Y. Zhang, S. Yan, Appl. Phys. Lett. **92**, 52508 (2008)

38. M. Gajdoš, K. Hummer, G. Kresse, J. Furthmüller, F. Bechstedt, Phys. Rev. B **73**, 45112 (2006)

39. J. Perdew, K. Burke, M. Ernzerhof, Phys. Rev. Lett. **77**, 3865 (1996)

40. J. Perdew, K. Burke, M. Ernzerhof, Phys. Rev. Lett. **78**, 1396 (1997)

41. A. Rohrbach, J. Hafner, G. Kresse, Phys. Rev. B **69**, 75413 (2004)

42. S. Baroni, R. Resta, Phys. Rev. B **33**, 7017 (1986)

43. F. Birch, Phys. Rev. **71**, 809 (1947)

44. A.K. Cheetham, D.A.O. Hope, Phys. Rev. B **27**, 6964 (1983)

45. F.A. Cotton, *Chemical Applications of Group Theory* (John Wiley and Sons Inc., New York, 1990)

46. J.E. Petersen, F. Twagirayezu, L.M. Scolfaro, P.D. Borges, W.J. Geerts, AIP Adv. **7**, (2017)

47. M.S. Dresselhaus, G. Dresselhaus, A. (Ado) Jorio, *Group Theory: Application to the Physics of Condensed Matter* (2008)

48. Y. Tokura, N. Nagaosa, Science **288**, 462 (2000)